CNRS

Centre National de la Recherche Scientifique

INFN

Istituto Nazionale di Fisica Nucleare

Evaluation of the quality factors of the mirrors in Advanced Virgo

VIR-0494A-17

Issue: 2

Date: April 02, 2019

Authors:

P. Puppo[1]

[1]*INFN, Sezione di Roma*

Abstract

In this note we present the computation of the mechanical Qs in the test masses of the Advanced Virgo interferometer and their thermal noise. The losses in the test masses are mainly due to the HR coatings on their front faces, however the effect of the bonding layers present in wire attachments systems and in the magnets can give a non-negligible effect that can influence the final losses of a few percent. We have developed a FE model with Ansys including all the mechanisms mentioned above. A study of the expected mirror losses with the steel suspension wires is also presented. In this note we also recall some results obtained during the study of the thermal noise in the interferometer Virgo+. The results are useful to have some hints for the Advanced Virgo thermal noise prediction.

1 The Advanced Virgo test masses

The Advanced Virgo test masses have a mass of 42 kg, on their lateral sides there are fused silica interface pieces called ears which are used for the monolithic suspension system with fused silica wires (see Figure 1-1). For this reason, the ears have slots which allow the fiber, having a T-shaped attachment piece at the bottom (anchor), to be slotted in and connected to the ear in compressive load. The ears are fixed to the test mass sides by silicate bonding (hydroxide-catalysis bonding) and the anchors are fixed to the ears with same method, forming a quasi-monolithic final stage. This method of attachment allows the low mechanical loss of the mirror to be preserved by eliminating the use of higher loss metal wires and the consequent losses due to the frictions and slippages in the coupling points with the test masses (spacers and break-off points).

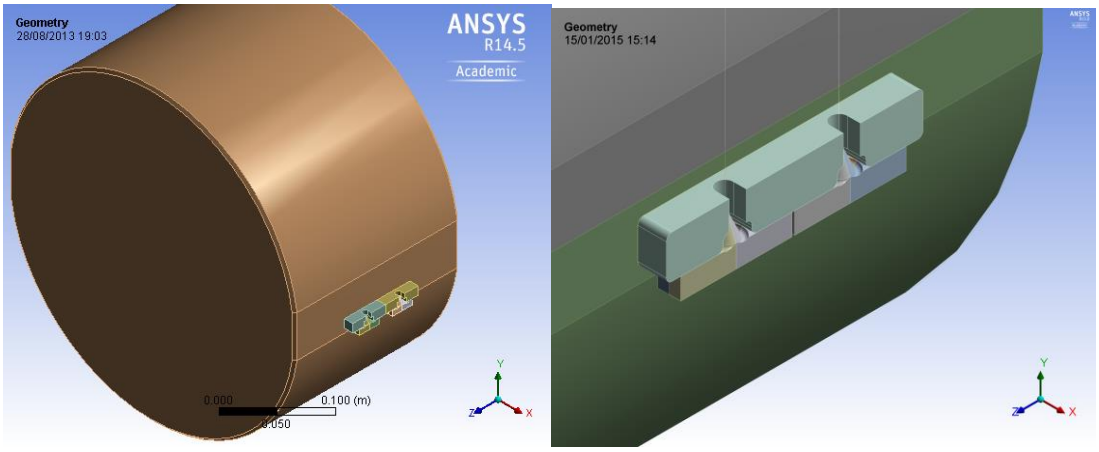

Figure 1-1: Advanced Virgo test mass and its clamping system

Because of the failures occurred on the silica suspension, in a first phase, the Advanced Virgo mirrors will be suspended with steel wires. For this reason, 4 spacers have been attached on the lateral sides of the test masses in order to allow the steel wires to pass over the ears and to be positioned at the correct distance (see Figure 1-2). The spacers are attached with the silica bonding technique, so also the layers of these bonds are in included in the model for the losses computation.

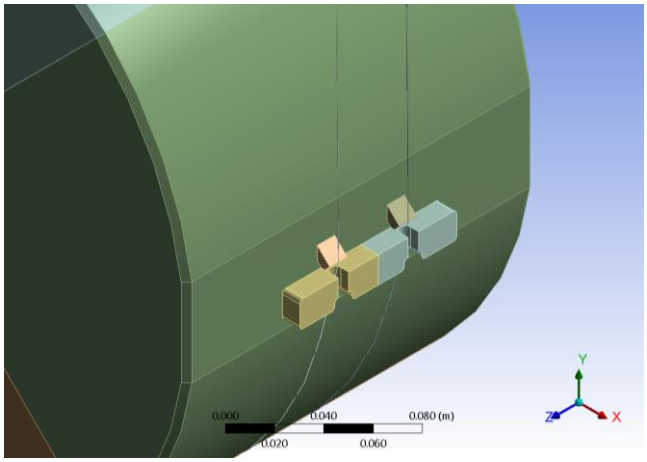

Figure 1-2: Detail of the suspension with the steel wires.

1.1.1 The ears and anchors design

The fused silica ears and anchors provide an appropriate interface to couple the fibers to the mirror lateral sides via the hydroxide-catalysis bonds. The criteria used to make an optimized design of the interface standoff pieces are that the ears must provide a safe interface between the mass and the fibers with a minimum safety factor of 3 in strength. Moreover, the thermal noise level for a single test mass resulting from ears and anchors attachment bonds must be lower than the mirror thermal noise level due to its internal and coating losses.

In Virgo+ the anchors were attached to the ears with a "soft silicate bonding" ($Na_2Si_3O_7$ water solution)[45] (previously named as 'water glass'), a solution more similar to a commercial glue in the bonding procedure, which permits to easily detach them from the ears in case of failure. For this reason, the geometry of the anchors is optimized for this purpose. Those zones attached in this way had a lower breaking strength with respect the hard silicate bonded one and can be more dissipative than that one.

In Advanced Virgo, it has been decided to attach the anchors with the same silicate bonding type as for the ears, so, although a bigger force is needed to detach the anchors in case of failure, a low mechanical dissipation is ensured.

We are aware that coating losses dominate in current estimates of the thermal noise, however we have paid some attention on the losses that can be introduced by the presence of the silicate bonding zones.

The finite element model is very useful also to understand if the dissipations in the bonded zones of the ears, anchors and spacers can spoil the test mass and wires loss angles and, in case, to have indications in the optimization of their design.

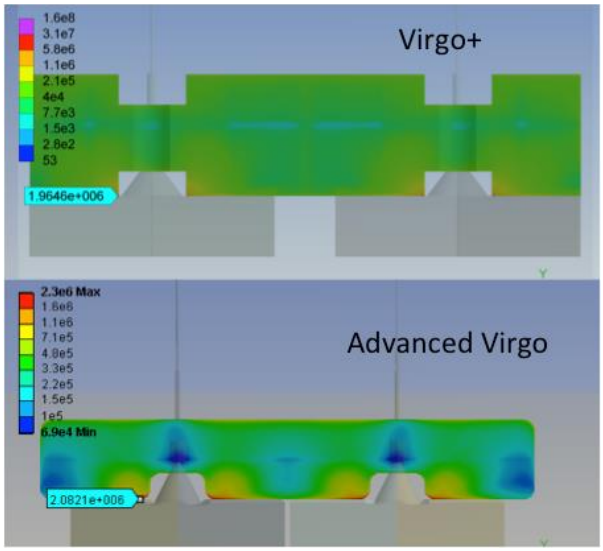

Figure 1-3: Study of the stress (Pa) distribution on the bonds. The optimization was perfomed by designing round edges on the ears in the Advanced Virgo clamps.

In Advanced Virgo the anchors and ears design were optimized to keep the bonded interface stresses within the safety levels already experienced and tested for the Virgo+ monolithic suspensions. To this aim the design of the ears are similar to Virgo+ and are attached with hard silicate bonding having a breaking strength of about 6 MPa, while the anchors are shaped to allow an easier detachment in case of wire failure and attached with soft silicate bonding [3][4] (see Figure 1-3). Also the spacers, adopted in the configuration with the steel wires suspension are attached softly to allow an easy detachment when we will pass to the monolithic suspension.

2 Dissipation angles and thermal noise calculations using ANSYS program

The quality factor of the mirror modes can be calculated taking into account all the dissipation mechanisms present on the test mass. We have that the total loss angles can be written as:

$$\phi_{overall} = \sum \phi_i \frac{E_i}{E_{tot}} =$$

$$= \phi_{material} + \phi_{coat} \frac{E_{coat}}{E_{tot}} + \phi_{layers} \frac{E_{layers}}{E_{tot}} + \phi_{magnets} \frac{E_{mags}}{E_{tot}} + \phi_{spacers} \frac{E_{spacers}}{E_{tot}} + \cdots$$

where E_i are the strain energies stored at a given frequency by the dissipative volume with loss angle ϕ_i so that the ratios $\frac{E_i}{E_{tot}}$ are the dilution factors of each loss mechanism.

With aid of the FEM we can calculate the dilution factors for each mechanism in the model, and then give the prediction of the quality factor at a given frequency. Of course, the accurate knowledge of the loss angles makes accurate also the prediction of the Qs.

Thermal noise can be calculated using the method proposed by Levin[13]. The average dissipated power, W_{diss}, caused by deformation of test mass by a notional force, F_0, associated with a test pressure having the same spatial distribution as the laser cross section at measurement frequency

f and temperature T, is proportional to the thermal noise power spectrum, outside the resonance zones, through the equation:

$$S_X^{Levin}(\omega) = \frac{4\,k_b T}{\omega^2 F_o^2}\,2\,W_{diss}$$

The dissipated power can be expressed as function of strain energy, ε, and loss factor, ϕ

$$W_{\text{diss}} = 2\pi f \int_{\text{vol}} \varepsilon(x,y,z)\,\phi(x,y,z)\,dV$$

The finite element analysis package ANSYS Workbench® is used to calculate the strain energy density $\varepsilon(x,y,z)$ of elastic deformation of a test mass driven by an oscillating Gaussian pressure of peak force magnitude F_0. The average dissipated power is then obtained from the integral of this energy density multiplied by the mechanical loss (which is inhomogeneous) over the volume of the mass. The thermal noise contribution is thus obtained from the average dissipated power using the fluctuation-dissipation theorem.

We note that this expression holds in the off-resonances zones and can be used also for the suspension thermal noise outside the pendulum frequency. To validate the model, we have calculated the thermal noise of the simple mirror four-wires suspension using the strain energies of the wires and the mirror given by ANSYS, through the expression:

Equation 2-1

$$S_X^{FEM}(\omega) = \frac{4\,k_b T}{\omega\,F_o^2}\,2\,\left(\phi_{wires}(\omega)E_{wires}(\omega) + \phi_{mirror}E_{mirror}(\omega)\right)$$

where F_o is evaluated using the Ansys meshing on the mirror face as the sum:

$F_o = \sum_i^{surf\_elem} P_i\,A_i$ where $P_i = \frac{2}{\pi w_{beam}^2} e^{-2(x_i^2+y_i^2)/w_{beam}^2}$ is the applied gaussian pressure on the i_{th} facet at (x_i, y_i) on the mirror surface meshing with area A_i.

We have compared with the theoretical expression:

Equation 2-2

$$S_X^{FEM}(\omega) = \frac{4\,k_b T}{M\,\omega}\left(\frac{\phi_{wires}(\omega)\omega_p^2}{\left(\omega^2-\omega_p^2\right)^2+\left(\omega_p^2\phi_{wires}(\omega)\right)^2}\right)+\frac{4\,k_b T}{\omega\,F_o^2}\,2\phi_{mirror}E_{mirror}$$

The agreement is very good, so we have used this method for predicting the payload suspension thermal noise including all the dissipations present in the system.

In the plot shown in Figure 2-1 we can see that the pendulum thermal noise crosses the mirror thermal noise at a few tenths of Hertz, then it does not affect it above that frequency value. For this reason, to have an estimation of the overall mirror thermal, we have computed it without including the suspension system, and then we added it to the suspension thermal in a second step. This method is useful to save computing time and memory occupied by the solution.

The detailed mirror model includes the ears, the magnets, the anchors (or the spacers, in case of the steel wires suspensions) and their bonding layers, which can play an important role for the losses computation. It is calculated from 10 Hz up to a few kHz.

The suspension thermal is calculated from a few Hz up to about 100 Hz, and includes the mirror mass and the marionette mass with its wire. A difficulty in the evaluation of the suspension thermal noise is the estimation of the loss angles of the wire attachment systems both on the test

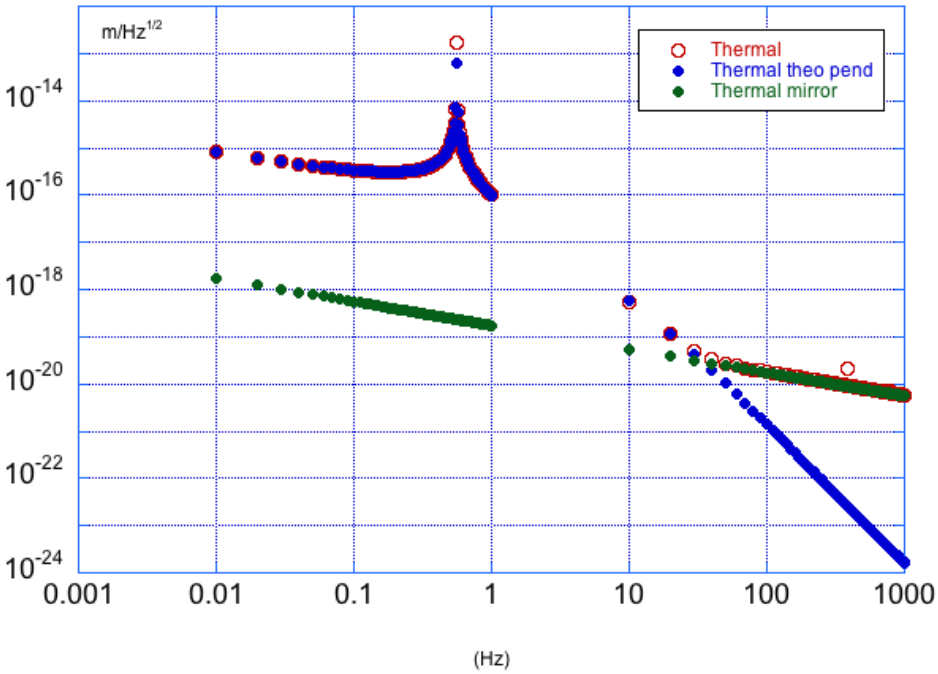

Figure 2-1: Thermal noise spectrum of a mirror suspended to four silica wires. The FEM result is compared with the pendulum thermal noise and the mirror bulk thermal noise. The agreement is optimal.

masses and the marionette. Such losses can affect the violin modes as well as the mirror quality factors. The measurements of the mechanical quality factors of the violin modes and of the mirror internal modes are used to make an estimation the loss factors by performing a fit with the Q's predicted by the FEM.

A lot of work has been already done in this direction showing some results (see notes [2],[10],[1]), deduced by a not yet complete FEM and based on the measurements performed on the payloads of the interferometer Virgo+. Here we want to give a wider and more complete analysis that it shows to be useful for a better comprehension of the results and to give a realistic prediction of the thermal noise in the Advanced Virgo suspension system.

3 The quality factors of the test masses.

The model of the test masses in Virgo includes the bonding layers and the HR coating on their front side. This model was used to calculate the quality factors limits on the mirror internal modes and the thermal noise limits due to such dissipations. The mechanical properties of the mirrors in Virgo+ and Advanced Virgo are given in the Table 3-1, Table 3-2 and Table 3-4.

3.1.1 Loss angles evaluations associated to the thin layers

The analysis method used is based on solid elements that, historically, are not well suited to representing very thin layers.
To this purpose, a preliminary work was carried out using shell elements to simulate the bond.
However, further work showed that shell elements are not suitable for modelling constrained surfaces because of the inability of shell elements to model shear stresses which are the dominant effect in the evaluation of the strain energy. This led to the development of a method which can accurately model very thin surfaces in solid elements.

	Virgo+	
	INPUT (North, West)	**END (North, West)**
Thickness (mm)	100.40, 99.25	99.95, 99.90
Diameter (mm)	350	350
Flats height (mm)	50	100
Mass (kg)($\pm 0.02\ kg$)	21.32, 21.07	
Material Properties	$\rho = 2202\ kg/m^3$ $Y = 72.3\ GPa$ $\sigma = 0.17$	

	Advanced Virgo	
	ITM	**ETM**
Thickness (mm)	200	200
Diameter (mm)	350	350
Flats height (mm)	50	50
Mass (kg)($\pm 0.02\ kg$)	42.3	42.3
Material Properties	$\rho = 2202\ kg/m^3$ $Y = 72.3\ GPa$ $\sigma = 0.17$	

Table 3-1: Data used in the FEM of the test masses

The technique used in the note [1] to solve this problem relied on an extrapolation from much thicker bond regions. By plotting the thermal noise against thickness, it was possible to get and approximation of the thermal noise at much lower thicknesses than were measurable.
However, this technique relies on the linear dependency with thickness that is not verified in all the cases. This could allow a correct extrapolation at the desired values only in those cases where the bonding area is smaller with respect to the area where it is attached, or in the case of the coatings where the shear deformation is not dominant.

Recently, with the Ansys Workbench mesh tools it is possible to model the thin bond layers by using a swept mesh to circumvent this problem. A swept mesh uses a 2-D mesh on one surface which is then extended through the body, the size parameters for the surface mesh and the number of layers can be specified by the user so avoiding the usual mesh limitations. Although the bond area is being modeled using very highly deformed elements, comparisons with analytical calculations for simpler cases give weight to the simulation results using this novel method [15] .

With ANSYS Workbench® it is also possible to calculate the strain energy density U of elastic deformation associated to the internal mode shapes to foresee the losses at these frequency values. The loss angle of a layer, is related to the fractional energy in that volume lost during the mode oscillation and can be written using the formula:

$$\Phi_{layer}(\omega_{mode}) = \frac{U_{layer}}{U_{tot}}\varphi_{layer}$$

being U_{layer} the strain energy in the layer volume, $U_{tot}$the overall strain energy of the mode and φ_{layer} the material loss term.

3.2 Coating modal losses and thermal noise

The coating multilayer is treated as a composite material characterized by effective properties defined in the following formulas [16]:

$$Y_{eff} = \frac{Y_L h_L + Y_H h_H}{h_L + h_H}$$

$$\sigma_{eff} = \frac{\sigma_L Y_L h_L (1-\sigma_L^2) + \sigma_H Y_H h_H (1-\sigma_H^2)}{Y_L h_L (1-\sigma_L^2) + Y_H h_H (1-\sigma_H^2)}$$

$$\rho_{eff} = \frac{\rho_L h_L + \rho_H h_H}{h_L + h_H}$$

$$\varphi_{eff} = \frac{\varphi_L h_L Y_L + \varphi_H h_H Y_H}{h_L Y_L + h_H Y_H}$$

Equation 3-1

Where the subscripts 'L' and 'H' refer to the low and high refraction index materials (silica and Tantala pentoxide) respectively.
The properties of the high index material can be calculated taking into account the amount of Titania doping in it, through the expressions:

$$Y_H = \frac{Y_{Ta} Y_{Ti}}{Y_{Ta} t_{Ti} + Y_{Ti} t_{Ta}}$$

$$\sigma_H = \frac{\sigma_{Ta} Y_{Ta} t_{Ta} (1-\sigma_{Ta}^2) + \sigma_{Ti} Y_{Ti} t_{Ti} (1-\sigma_{Ti}^2)}{Y_{Ta} t_{Ta} (1-\sigma_{Ta}^2) + Y_{Ti} t_{Ti} (1-\sigma_{Ti}^2)}$$

$$\rho_H = \frac{\rho_{Ta} t_{Ta} + \rho_{Ti} t_{Ti}}{t_{Ta} + t_{Ti}}$$

Equation 3-2

where the properties of the materials are given in the Table 3-2.
In the model a very dense meshing was used in the bonded zone.
To calculate the thermal noise the beam induced deformation of test mass was performed with a 1 N normalized force and a Gaussian profile with the waist values given in the Table 3-1. The results are given in the Table 3-3.

Virgo+ Mirrors				
Coating Properties			**INPUT (North, West)**	**END (North, West)**
	Coating Diameter (mm)		200	330
High index material (Ti:Ta_5O_2) $\varphi = (2.4 \pm 0.4)\ 10^{-4}$	(Ta_5O_2)	$\rho_{Ta} = 6850\ kg/m^3$ $Y_{Ta} = 140\ GPa$ $\sigma_{Ta} = 0.23$ $t_{Ta} = 67\ \%$	$\rho_H = 5995.3\ kg/m^3$ $Y_H = 214\ GPa$ $\sigma_H = 0.255$	$\rho_H = 5995.3\ kg/m^3$ $Y_H = 214\ GPa$ $\sigma_H = 0.255$
	Doping material (Ti)	$\rho_{Ti} = 4260\ kg/m^3$ $Y_{Ti} = 290\ GPa$ $\sigma_{Ti} = 0.28$ $t_{Ti} = 33\ \%$		
Low Index Material (SiO_2) $\varphi = (4.6 \pm 0.1)10^{-5}$			$\rho_L = 2202\ kg/m^3$ $Y_L = 72\ GPa$ $\sigma_L = 0.17$	$\rho_L = 2202\ kg/m^3$ $Y_L = 72\ GPa$ $\sigma_L = 0.17$
	(Ti:Ta_5O_2) Thickness		0.771 μm	2.699 μm
	(SiO_2) Thickness		1.210 μm	4.055 μm
	Effective properties (See Formulas) and calculated losses		$\rho_{eff}^{ITM} = 3678.23\ kg/m^3$ $Y_{eff}^{ITM} = 109.7\ GPa$ $\sigma_{eff}^{ITM} = 0.194$ $\varphi_{eff}^{ITM} = 1.62\ 10^{-4}$	$\rho_{eff}^{ETM} = 3717.6\ kg/m^3$ $Y_{eff}^{ETM} = 110.7\ GPa$ $\sigma = 0.223$ $\varphi_{eff}^{ETM} = 1.64\ 10^{-4}$

Table 3-2: Coating properties for Virgo+ mirrors

	INPUT MIRROR				END MIRROR			
Coating Losses								
	Frequency (Hz)	$\frac{U_{ITM}}{U_{tot}}$	φ_{ITM}	Q_{ITM} (10^6)	Frequency (Hz)	$\frac{U_{ETM}}{U_{tot}}$	φ_{ETM}	Q_{ETM} (10^6)
Butterfly (1,2)	3966-3998	$4.1\ 10^{-5}$	$6.7\ 10^{-9}$	150	3938-3983	$2.6\ 10^{-4}$	$4.2\ 10^{-8}$	24
Drum	5677	$5.2\ 10^{-5}$	$8.6\ 10^{-9}$	120	5647	$2.9\ 10^{-4}$	$4.6\ 10^{-8}$	22
Butterfly (3,4)	7641-7712	$2.0\ 10^{-5}$	$3.3\ 10^{-9}$	300	7595-7684	$2.3\ 10^{-4}$	$3.8\ 10^{-8}$	26
Coating Thermal Noise (1 Mirror)								
	Beam Waist	$\frac{U_{ITM}}{U_{tot}}$	φ_{ITM}	Thermal Noise $m/\sqrt{Hz}$	Beam Waist	$\frac{U_{ETM}}{U_{tot}}$	φ_{ETM}	Thermal Noise $m/\sqrt{Hz}$
@100 Hz *(with Gaussian pressure)*	2.25 cm half-width	$0.84\ 10^{-4}$	$1.4\ 10^{-8}$	$1.1\ 10^{-20}$	5.5 cm half-width	$2.2\ 10^{-4}$	$3.5\ 10^{-8}$	$1.1\ 10^{-20}$

Table 3-3: FEM results for coating losses in Virgo+ mirrors

Advanced Virgo Mirrors				
Coating Properties			**INPUT (North, West)**	**END (North, West)**
	Coating Diameter (mm)		350	350
High index material (Ti:Ta_5O_2) $\varphi = (2.4 \pm 0.4)\ 10^{-4}$	(Ta_5O_2)	$\rho_{Ta} = 6850\ kg/m^3$ $Y_{Ta} = 140\ GPa$ $\sigma_{Ta} = 0.23$ $t_{Ta} = 67\ \%$	$\rho_H = 5995.3\ kg/m^3$ $Y_H = 214\ GPa$ $\sigma_H = 0.255$	$\rho_H = 5995.3\ kg/m^3$ $Y_H = 214\ GPa$ $\sigma_H = 0.255$
	Doping material (Ti)	$\rho_{Ti} = 4260\ kg/m^3$ $Y_{Ti} = 290\ GPa$ $\sigma_{Ti} = 0.28$ $t_{Ti} = 33\ \%$		
Low Index Material (SiO_2) $\varphi = (4.0 \pm 0.1)10^{-5}$			$\rho_L = 2202\ kg/m^3$ $Y_L = 72\ GPa$ $\sigma_L = 0.17$	$\rho_L = 2202\ kg/m^3$ $Y_L = 72\ GPa$ $\sigma_L = 0.17$
	(Ti:Ta_5O_2) Thickness		$1.05\ \mu m$	$2.61\ \mu m$
	(SiO_2) Thickness		$1.64\ \mu m$	$3.83\ \mu m$
	Effective properties (See Formulas) and calculated losses		$\rho_{eff}^{ITM} = 4016.3\ kg/m^3$ $Y_{eff}^{ITM} = 98.5\ GPa$ $\sigma_{eff}^{ITM} = 0.203$ $\varphi_{eff}^{ITM} = 1.45\ 10^{-4}$	$\rho_{eff}^{ETM} = 4085.8\ kg/m^3$ $Y_{eff}^{ETM} = 99.6\ GPa$ $\sigma = 0.204$ $\varphi_{eff}^{ETM} = 1.48\ 10^{-4}$

Table 3-4: Advanced Virgo Mirrors Coating properties

	INPUT MIRROR				END MIRROR		
Coating Losses							
	Frequency (Hz)	$\frac{U_{ITM}}{U_{tot}}$	φ_{ITM}	Q_{ITM} (10^6)	$\frac{U_{ETM}}{U_{tot}}$	φ_{ETM}	Q_{ETM} (10^6)
Butterfly (1,2)	5735-5740	$4.7\ 10^{-5}$	$6.8\ 10^{-9}$	146	$1.1\ 10^{-4}$	$1.7\ 10^{-8}$	60
Drum	7842	$5.2\ 10^{-5}$	$7.5\ 10^{-9}$	133	$1.2\ 10^{-4}$	$1.8\ 10^{-8}$	54
Butterfly (3,4)	9933-9951	$4.6\ 10^{-5}$	$6.7\ 10^{-9}$	150	$1.1\ 10^{-4}$	$1.6\ 10^{-8}$	61
Coating Thermal Noise (1 Mirror)							
	Beam Waist	$\frac{U_{ITM}}{U_{tot}}$	φ_{ITM}	Thermal Noise $m/\sqrt{Hz}$	Beam Waist	$\frac{U_{ETM}}{U_{tot}}$	φ_{ETM}	Thermal Noise $m/\sqrt{Hz}$
@100 Hz *(with Gaussian pressure)*	4.87 cm half-width	$6.1\ 10^{-5}$	$8.9\ 10^{-9}$	$5.2\ 10^{-21}$	5.8 cm half-width	$1.5\ 10^{-4}$	$2.2\ 10^{-8}$	$8.1\ 10^{-21}$

Table 3-5: FEM results for coating losses in Advanced Virgo mirrors

There is a difference between the gwinc code [24] and the FEM outputs. Referring to the Figure 3-1, the gwinc evaluation (using the coating model) for the Advanced Virgo mirror is about 15% lower than the FEM probably because there is a difference in the used parameters. We inserted the

effective elastic properties and loss angle defined in the formulas (Equation 3-1) using the doped high refraction index material properties (Equation 3-2) with a measured loss angle of 2.4 10^{-4}.

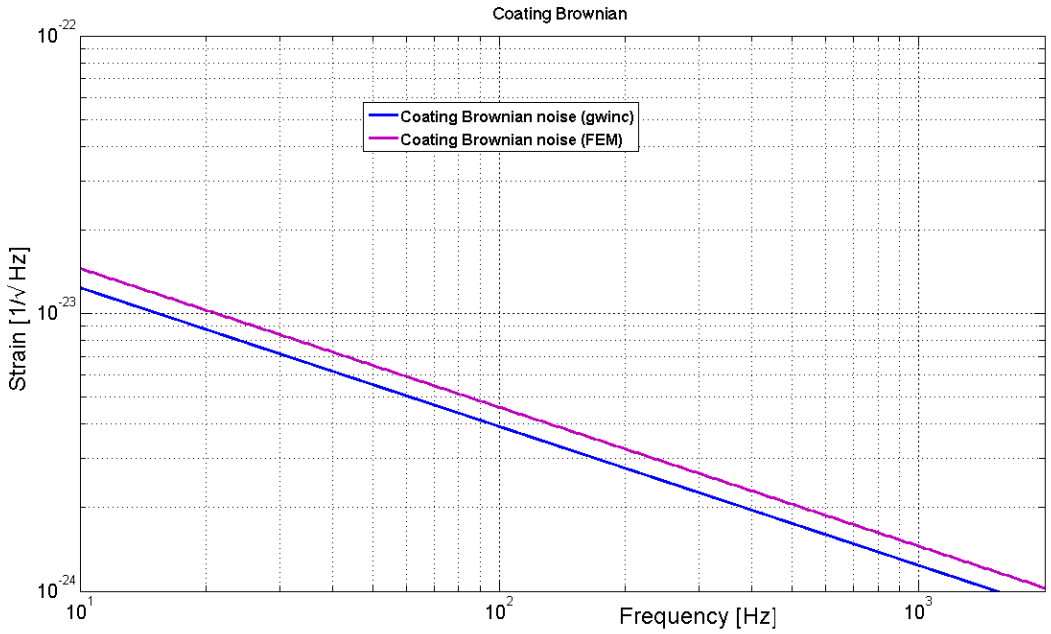

Figure 3-1: Coating Thermal Noise evaluated with the FEM of the mirror and with theoretical formulas in gwinc.

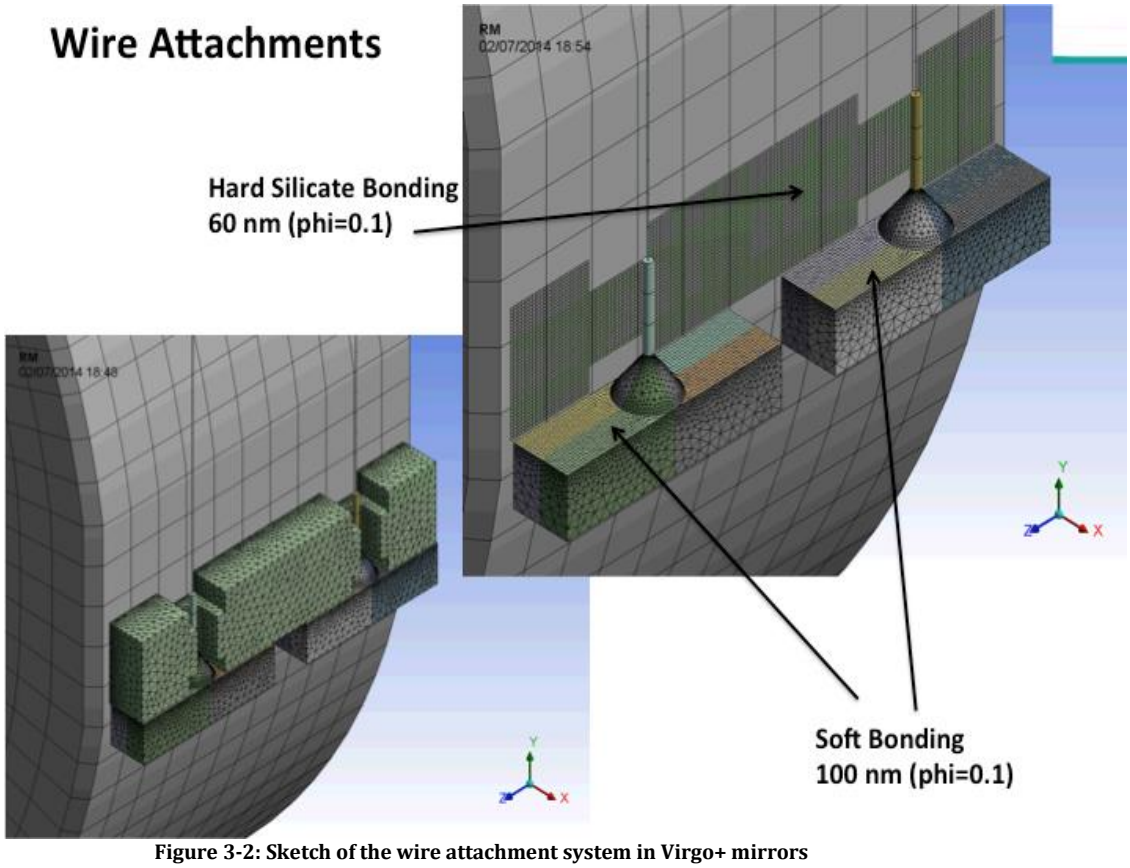

Figure 3-2: Sketch of the wire attachment system in Virgo+ mirrors

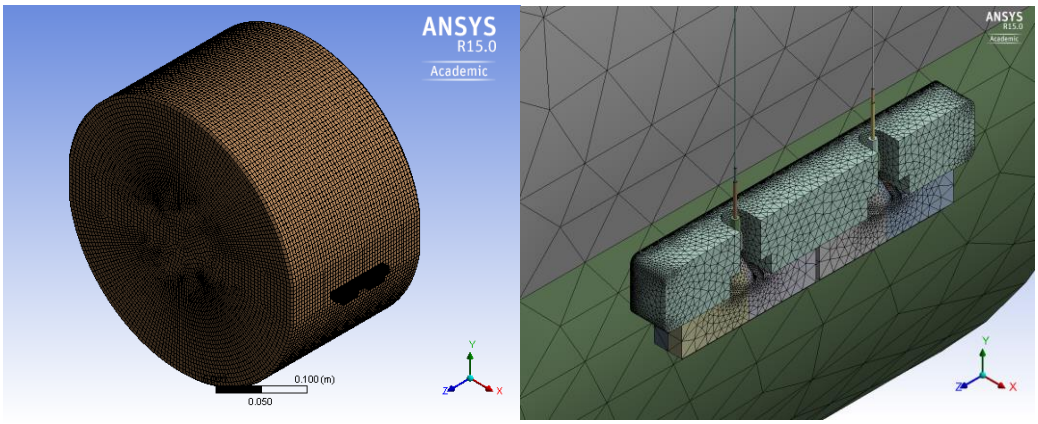

Figure 3-3: Advanced Virgo Test mass and the wires attachment system

3.3 Silicate bonded layers losses and thermal noise

The layers formed by the silicate bonded zone in the ears and in the anchors for the Virgo+ and Advanced Virgo mirrors are described in the Table 3-6 and Table 3-9. In our computation we have taken the bonding layers properties already presented in the paper [15] and in the note [2].

3.3.1 The case of Virgo+

For the mirror of Virgo+ the results of the simulation are shown in the Table 3-7. The curves are shown in the Figure 3-4 and compared with the mirror coating thermal noise. In the **Error! Reference source not found.** the expected overall quality factors and the overall thermal noise at 100 Hz are shown. In the **Error! Reference source not found.** the measurements of the Virgo+ mirrors quality factors are listed and in the **Error! Reference source not found.** a comparison with the FEM expectations is sketched.

We recall here some conclusions drawn from the analysis performed on the notes [1],[2],[10], and confirmed by the simulations.

1. The effect of the anchors attached with water glass is negligible in the mirror Qs;
2. The FE analysis results, together with the measurements in the laboratory confirm that the low Q of the WI mirror drum mode cannot be due to the water glass attaching the anchors. A possible explanation of such a low Q can be given by the interaction with the violin modes that can suck energy to the closer mirror mode lowering their Q. In particular, looking at the behavior of the Q of the violin modes in WI we observe that the quality factor reaches its minimum values at frequencies around the drum mode resulting in an accidental reduction of its quality factor. This behavior is present in all the mirrors, indeed all the drum modes have a quality factor lower than expected by the FE analysis and very close to the closest violin. In the NI mirror this effect shows up as a double frequency drum mode, while in the WI mirror it is impossible to resolve any mode degeneracy because of the very low Q.
3. The effect of the violin modes on the mirror Q was already observed in the past [11]. However, as shown in the case of the NI mirror on [1], the effects on the mirror thermal noise in the frequency range of 100 Hz are negligible like the interaction with the violins at those frequencies. For this reason a correct evaluation of the mirror thermal noise can be given by taking the loss angle extrapolated by the highest measured Q.

Ears	
Layer Thickness	60 nm
Bonded Area	$\mathbf{2 \times 16\ cm^2}$
Anchors	
Layer Thickness	100 nm
Bonded Area	$\mathbf{4 \times 3\ cm^2}$
Silicate Bonding	
Mechanical Properties	$\rho = 2200\ kg/m^3$ $Y = 7.9\ GPa$ $\sigma = 0.17$ $\phi = 0.1$

Table 3-6: Bonded zones in Virgo+ mirrors

	INPUT MIRROR			**END MIRROR**			
Bonding Losses							
	Frequency (Hz)	φ_{ITM}	Q_{ITM} (10^6)	Frequency (Hz)	φ_{ETM}		Q_{ETM} (10^6)
Butterfly (1,2)	3966 3998	$4.5\ 10^{-9}$ $7.2\ 10^{-9}$	220 140	3938 3983	$1.0\ 10^{-8}$ $1.5\ 10^{-8}$		100 68
Drum	5677	$3.2\ 10^{-9}$	310	5647	$5.5\ 10^{-9}$		180
Butterfly (3,4)	7641 7712	$8.4\ 10^{-9}$ $1.3\ 10^{-8}$	120 76	7595 7684	$2.1\ 10^{-8}$ $2.6\ 10^{-8}$		48 38
Bonding Thermal Noise (1 mirror)							
	Beam Waist	$\frac{U_{ITM}}{U_{tot}}$	φ_{ITM}	Thermal Noise $m/\sqrt{Hz}$	Beam Waist	$\frac{U_{ETM}}{U_{tot}}$	φ_{ETM}	Thermal Noise $m/\sqrt{Hz}$
@100 Hz *(with Gaussian pressure)*	2.25 cm half-width	$5.5\ 10^{-9}$	$5.5\ 10^{-10}$	$2.3\ 10^{-21}$	5.5 cm half-width	$2.5\ 10^{-8}$	$2.5\ 10^{-9}$	$3.1\ 10^{-21}$

Table 3-7: FEM results for bonding layer losses in Virgo+ mirrors.

In the Figure 3-4 we show a comparison between the thermal noise of the mirror coating and that one due to the bonding layers on the mirror. The computation was performed with the Levin method explained in the paragraph 2, using the calculation of the strain energy vs frequency obtained by the FEM model.

A technical remark is that in this kind of calculation we do not use the modal expansion method because it is limited by the number of modes previously computed with the modal analysis, but we used the full method.

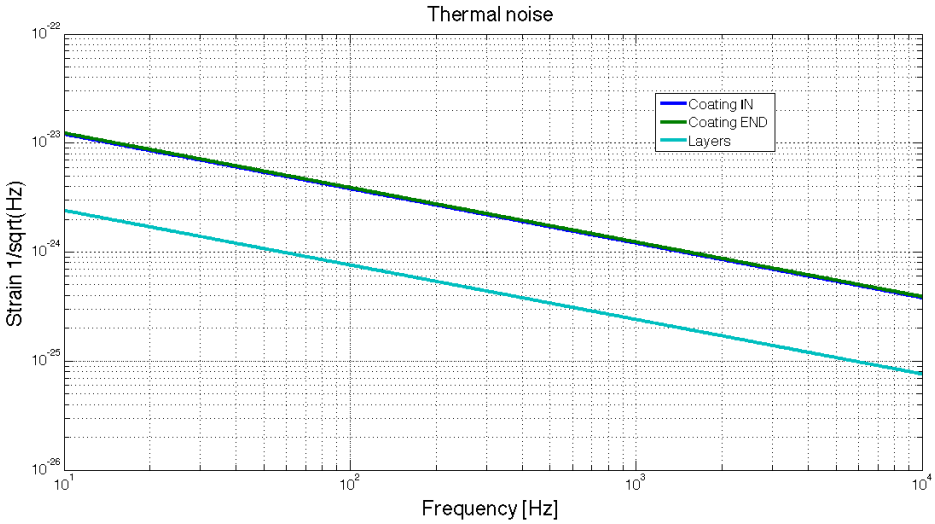

Figure 3-4: Virgo+ coating and silicate bonding layers thermal noise in comparison.

	INPUT MIRROR		**END MIRROR**	
Total				
	Frequency (Hz)	Q_{ITM} (10^6)	Frequency (Hz)	Q_{ETM} (10^6)
Butterfly (1,2)	3966 3998	87 67	3938 3983	19 17
Drum	5677	83	5647	19
Butterfly (3,4)	7641 7712	80 53	7595 7684	16 15
Total Thermal				
	Beam Waist	Thermal Noise $m/\sqrt{Hz}$	Beam Waist	Thermal Noise $m/\sqrt{Hz}$
@100 Hz *(with Gaussian pressure)*	2.25 cm half-width	$1.1\ 10^{-20}$	5.5 cm half-width	$1.2\ 10^{-20}$

Table 3-8: Overall quality factors and thermal noise at 100 Hz for the Virgo+ mirrors

3.3.2 Advanced Virgo

We have computed the quality factors and the thermal noise for the Advanced Virgo test masses. Only the modes with a frequency below 10kHz are shown in the tables however a more extensive calculation has been performed up to 80kHz (see paragraph 6). The results are useful for study the coupling between the mechanical modes and the optical modes and have an estimation of the of the parametric instabilities in the interferometer.

Ears	
Layer Thickness	60 nm
Bonded Area	$\mathbf{2 \times 12.5\ cm^2}$
Anchors	
Layer Thickness	60 nm
Bonded Area	$\mathbf{4 \times 1.6\ cm^2}$
Magnets	
Layer Thickness	60 nm
Bonded Area	$\mathbf{4 \times}$ ***diameter 6 mm***
Soft Silicate Bonding	
Mechanical Properties	$\rho = 2200\ kg/m^3$ $Y = 7.9\ GPa$ $\sigma = 0.17$ $\phi = 0.1$

Table 3-9: Bonded zones in the Advanced Virgo mirrors

Overall Bonding Layer Losses		
	Frequency (Hz)	Q_{TM} (10^6)
Butterfly (1,2)	5701-5704	100,1600
Drum	7797	760
Butterfly (3,4)	9856-9866	142-73.6
Layers Thermal Noise (1 Mirror) @ 100Hz		
Overall (magnets+anchors+ears)	$1.2\ 10^{-21}\ m/\sqrt{Hz}$	
Overall for steel susp. (magnets+spacers+ears)	$1.0\ 10^{-21}\ m/\sqrt{Hz}$	
Ears	$0.9\ 10^{-21}\ m/\sqrt{Hz}$	
Anchors	$0.6\ 10^{-21}\ m/\sqrt{Hz}$	
Magnets	$0.36\ 10^{-21}\ m/\sqrt{Hz}$	
Spacers	$0.34\ 10^{-21}\ m/\sqrt{Hz}$	

Table 3-10: Calculated losses and thermal noise related to the bonding layers on the Advanced Virgo Test Masses. If the steel suspensions are adopted the anchors are not present but the spacers layer losses must be included. In this case the overall thermal noise is slightly different.

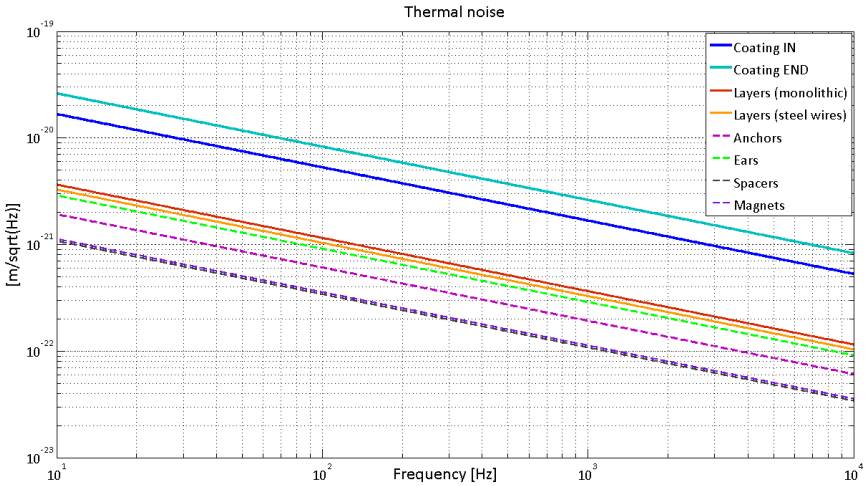

Figure 3-5: Plot of the thermal noises generated by the layers and the coatings in the test masses of AdV.

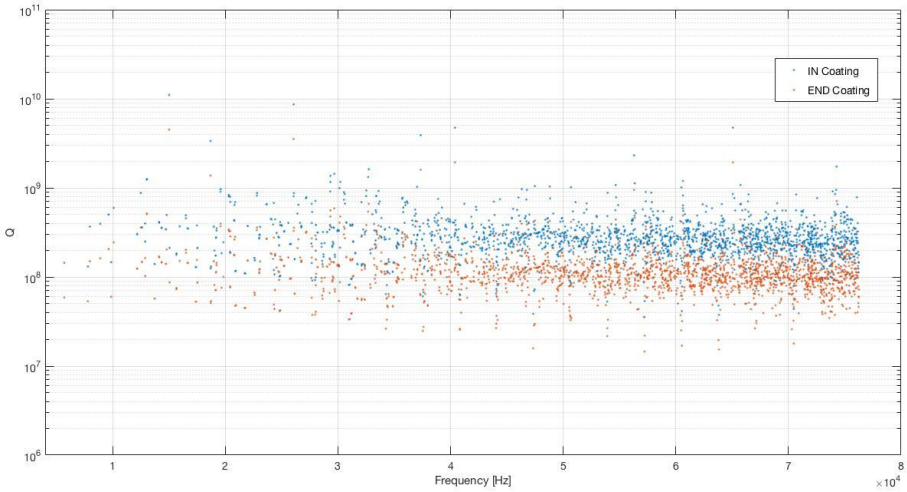

Figure 3-6: Q of Advanced Virgo mirrors due to the coating losses.

3.4 Suspended test masses FE model

The finite element model of the payload last stage suspension includes the marionette, the monolithic suspension of the mirror and, in the case of Virgo+, also the reaction mass. The clamps on the marionette are included in detail to evaluate the thermal noise contribution of these elements.

3.5 Virgo+ payload

The model was used to calculate the quality factor of all the modes of the overall system and then to compare them with the measurements on Virgo+. The results of such a comparison were very crucial to make an extrapolation of the dominant losses in Virgo+ and were helpful for an optimization of the payload design in Virgo Advanced.

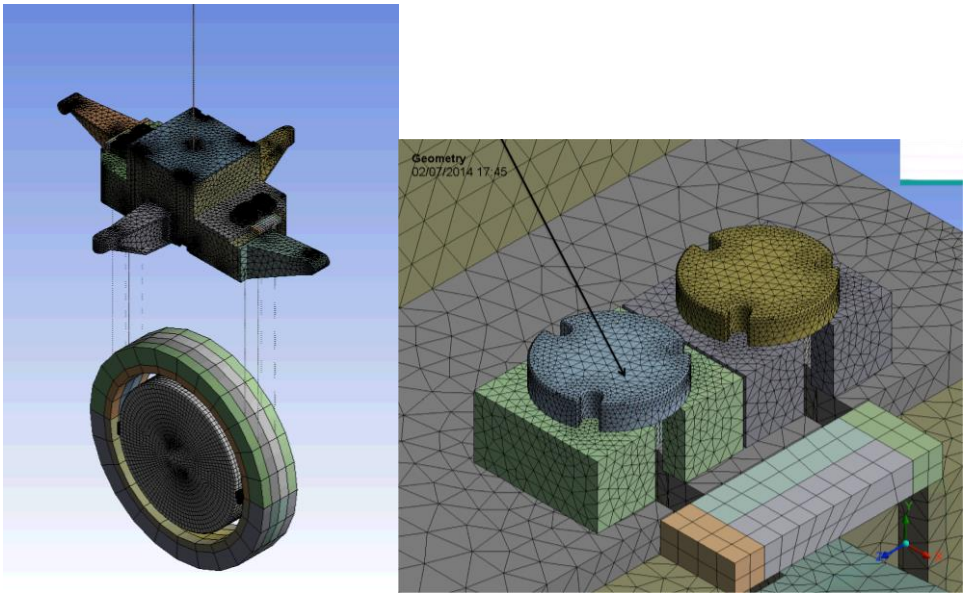

Figure 3-7: FEM model of the Virgo+ payload and upper clamp details of the simulation.

We have simulated the complete payload of the Virgo+ mirrors including the bond layers, the coating and the upper clamps detail as shown in the figure. The reaction mass geometry was simplified as we are not interested to its internal modes, and to the violin modes of its suspension wires. In the Figure 3-7 the fiber upper clamps model is shown in detail.

The overall quality factor is calculated by the formula:

Equation 3-3

$$Q_{tot} = \left(\frac{1}{Q_{TMwires}} + \frac{1}{Q_{RMwires}} + \frac{1}{Q_{UpClamps}} + \frac{1}{Q_{DownClamps}} + \frac{1}{Q_{mario}} \right)$$

Each term influences also the frequency behavior of the Qs, and it is given by the expression

$$Q_i = \left(\phi_i \frac{U_i}{U_{tot}} \right)^{-1}$$

ϕ_i are the loss angles of each payload component. The influence of the reaction mass is mainly due to its recoil via the suspension wires and is present only in the pendulum modes of the payloads. For this reason, in this analysis we kept only the loss term due to the steel wires suspending the reaction mass and we have neglected its mass term. Its values were extrapolated from the Q of the pendulum modes.

U_i and U_{tot} are the taken by the output of the FEM analysis.

The quality factor of the lower clamps contains the bond layers on the mirrors used to attach the anchors and the ears. For the bond layers we have used the loss angles shown in the Table 3-6.

With this model we were able to compute the Qs of the violin modes up to the 20th order.

During the measurements campaign on the violin modes of the Virgo+ payloads, a deep analysis of the results were performed and from the FEM model we were able to extrapolate the loss angles of all the contributors for each payload. The results are shown in the Table 3-11.

The comparison with the measured ones in shown in the Figure 3-9 (NI case). We notice that from the violin modes is also possible to extrapolate the effective loss angle of the marionette

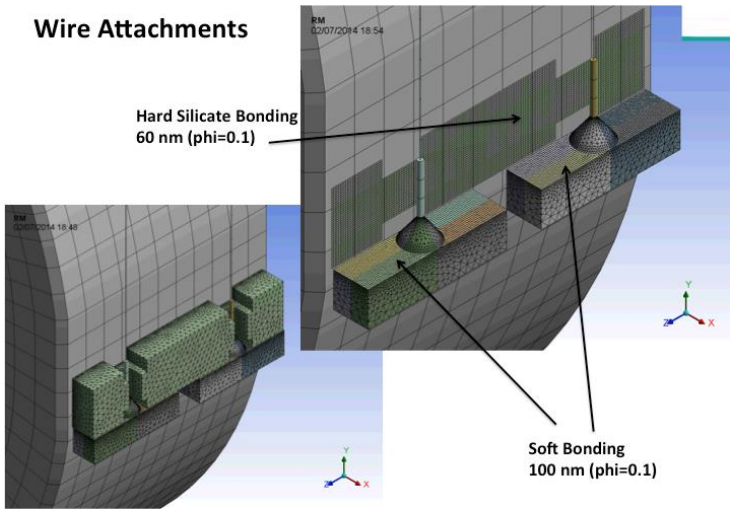

Figure 3-8: System of clamping of the silica wires to the lateral side of the mirror. The T-shaped wire ends are attached to the ears through the soft silicate bonding. The ears are attached to the mirror flats with hard silicate bonding. Their properties are summarized in the Table 3-9

body which is of the order of 10^{-3}. The marionette can influence the violins Q frequency behavior above 5 kHz.

	NI	WI	NE	WE
ϕ_{mario}	$8\ 10^{-3}$	$1\text{-}5\ 10^{-3}$	$4\ 10^{-3}$	$1\ 10^{-4}$
$\phi_{UpClamps}$	$1.1\ 10^{-4}$	$1\ 10^{-4}$	$1.3\ 10^{-4}$	$5\ 10^{-4}$
$\phi_{RMWires}$	$1\ 10^{-3}$	$2\ 10^{-4}$	$2\ 10^{-3}$	$4\ 10^{-4}$

Table 3-11: Extrapolated loss angles in the Virgo+ payloads.

This role of each payload suspension part is shown in the Figure 3-10 where the quality factors of the bond layers (orange dots) and of the silica wires (green dots) are plotted in comparison with to the overall Qs (red dots). It is evident that the bond layers Qs are higher than the wires ones and then their contribution is negligible. The agreement between the violin modes measurements (blue dots) and the prediction can be found if **the main dissipative mechanism in the suspension system is attributed to the clamps on the marionette.**

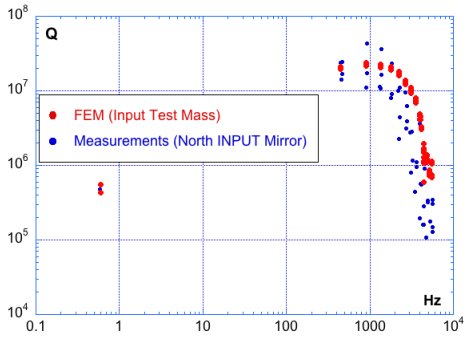

Figure 3-9: Plot of the predicted Q of the violin modes compared with the measured ones (NI payload case). The pendulum Q (below 1 Hz is useful to extrapolate the losses of the RM suspension wires)

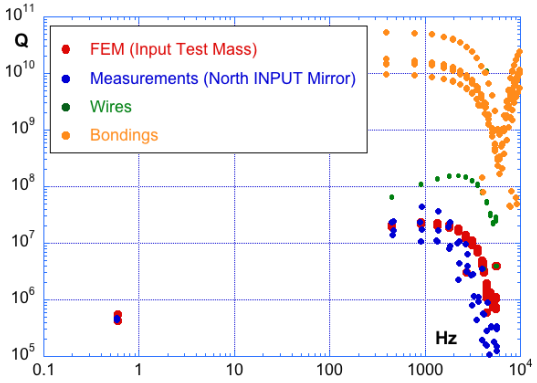

Figure 3-10: Q prediction of the violin modes in Virgo+: comparison between the various dissipative terms. An higher Q indicates low mechanical dissipation. The effect of the bond layer losses is negligible with respect to the other main dissipative element which is the clamping system on the marionette.

4 The coupling of the bulk modes and the violin modes

If a given mirror frequency is close to a violin mode, a coupling between them can be possible. This coupling occurs through the wire attachment point on the mirror lateral side. In this condition there is an energy transfer and the resulting mirror (and violin) Q can change with respect to the uncoupled status.

When there is a strong coupling between the modes, i.e. the two frequencies are equal, two normal modes appear, having a Q closer to the lowest one. In the note [1], paragraph 1.1.4, this effect was treated by using the double oscillator formalism and used to explain the behavior of the NI double drum mode (see the Figure 4-1). In that case the Q of the double coupled modes was around $3\ 10^5$ like the violins Qs around that frequency and much lower than the expected drum Q of about $8\ 10^7$. Despite the very low Q, it was demonstrated that such a coupling does not influence the thermal noise level in the frequency range below the affected bulk mode which then is already due to the mirror losses.

To better give an interpretation of the coupling between bulk and wire modes, we have performed a more detailed study using the FEM.

As a first step we have studied the Q behavior of a Virgo+ (100mm thick, 21 kg) mirror bulk modes by varying the four wires lengths (from 0.75m to 0.85m), consequently shifting the violin mode

frequencies of a few Hertz. We have supposed $\phi_{viol} = 10^{-6}$ and $\phi_{bulk} = 2.5\ 10^{-8}$ as uncoupled loss angles.

In the Figure 4-2 we have plotted the Q of the drum mode vs the frequency of the nearest violin mode. As soon as the frequency of the wire approaches the mirror drum the energy exchange becomes more and more strong so that the Q of the drum decreases until they are the tuned. This effect starts to be evident already at a few tenth of Hertz from the violin mode, and it shows up as a reduction of the mirror Q.

The mirror frequency shifts are normally observed in the interferometer and are correlated to the temperature changes in the towers, this behavior was also useful to identify the mirror lines in Virgo+ interferometer (see in [1]). Although the temperature is controlled and kept in the suspension halls within ± 1 °C, this small variation can result in modifying considerably the coupling between the mirror and the wire modes.

The elastic properties ($E_o = 72.2\ GPa, \sigma_o = 0.17$) modify with the temperature. For the fused silica we have that: $\frac{\Delta Y}{Y\,\Delta T} = 1.84 \cdot 10^{-4}\,\frac{1}{K}$ for the Young modulus and $\frac{\Delta \sigma}{\sigma\,\Delta T} = 2.5 \cdot 10^{-4}\ \frac{1}{K}$ for the

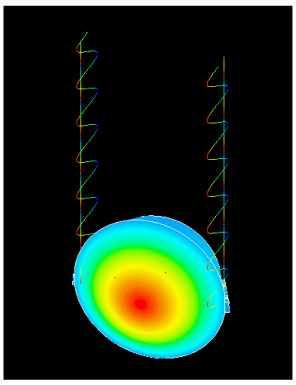

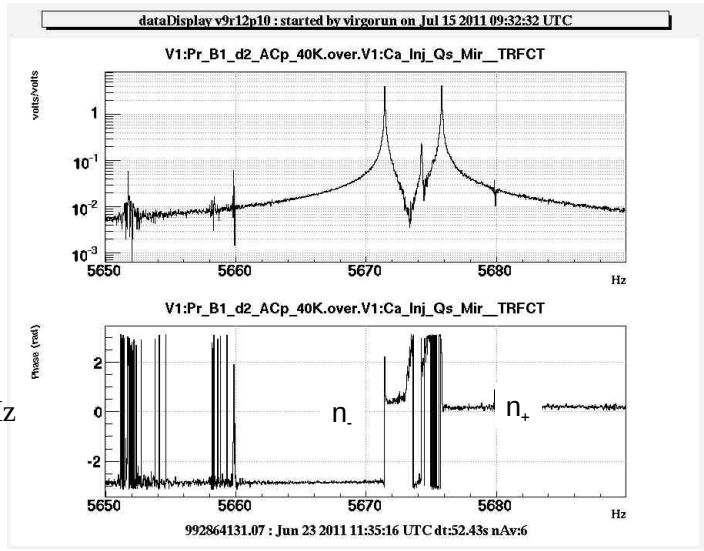

$n_- = 5671.8$ Hz ; $n_+ = 5676.2$ Hz

$$n_b = \frac{n_+ - n_-}{2} = \frac{n_o}{2}\sqrt{m}$$

$n_o = n_{XIII} = n_{drum} = 5674$ Hz

$m = M_{drum} / M_{XIII} = 6 \times 10^{-7}$

P. Rapagnani: Il nuovo Cimento v5, n4, 1982, p385

XIII violin - NI drum mode degeneracy
The lowest Q dominates

Figure 4-1: Case of the input test mass of the Virgo+ interferometer, North Arm. The coupling with the violin mode splits the drum mode into two frequencies. Their quality factors are lower. The XIII violin in the x direction is also present.

Poisson ratio giving [1] a shift coefficient of 0.6-0.8 Hz/K for the drum mode and much smaller for the wires (about 0.02 Hz/K).

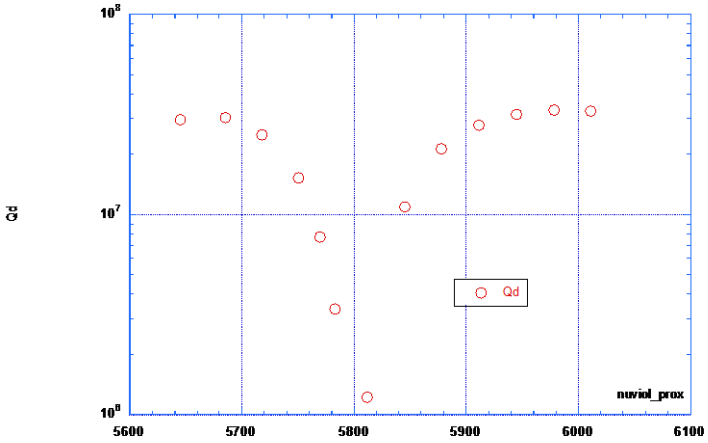

Figure 4-2: Q of the drum mode vs the frequency of the nearest violin mode. The minimum value is approached when the two mode have similar frequencies.

We have studied the coupling effect between the drum mode and the nearest violin mode by varying only the Young modulus for the Suprasil of the test mass, with the aim to reproduce a shift like that one observed in a Virgo+ suspended mirror. We have set different wires with slight difference in the diameters (250 um ,260 um ,270 um ,290 um). This set up was useful to study the coupling with only one wire and see this effect better. Moreover, this can be consistent with the real setup where the wires diameters are not completely equal.

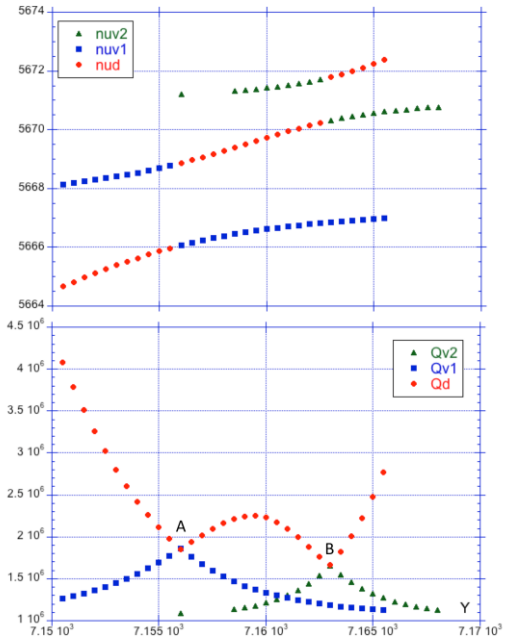

Figure 4-3: Evolution of the quality factor (lower plot) of three modes (drum (red dots) and two violins (blue squares and green triangles)) vs the Young Moduluss and their frequency evolution (upper plot).

We focused our attention to the case of the drum mode (5645 Hz with an uncoupled Q of 40 10^6) near the two XVth violin frequencies (5667.0 Hz, 5671.0 Hz with uncoupled Q of 10^6). In this study the wire loss angle is 10^{-6} and the bulk loss angle is 2.5 10^{-8}. The Young modulus varies from 71

GPa to 72 GPa. In Figure 4-3 the Q evolution of the three modes vs Y is plotted (zoomed around the tuning conditions). As soon as the Y value increases, the drum frequency increases approaching one violin. The quality factor of the drum (red dots) decreases (from a starting value of 5 10^7) and the violin mode Q (blue squares) increases till they coincide. After the first resonance the drum increases until it joins the other violin (green triangles) in a second resonance condition. At resonance the Q's coincide and are equal to about 2 10^6. In the Figure 4-4 the evolution of drum Q is plotted vs the difference between its frequency and the first uncoupled violin frequency. In this case the three modes have similar mode shapes and they are undistinguishable. We notice that also when the difference between the uncoupled modes is of few tenths of Hertz (see Figure 4-4) the quality factor of the drum mode is lower than its nominal value. This aspect suggests that we must be careful in using the measurements of Q of the mirror bulk modes to draw their loss angle.

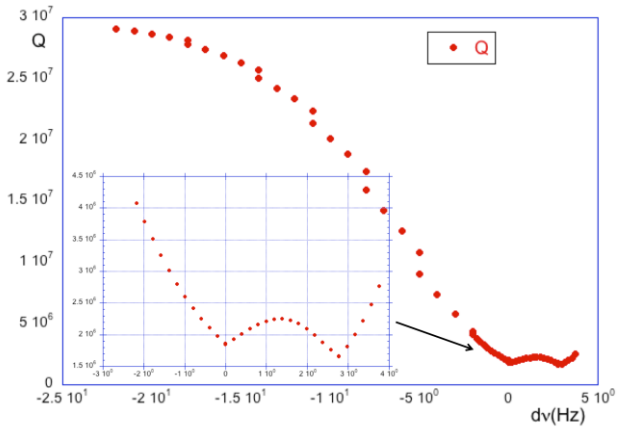

Figure 4-4: Q of the drum mode vs the difference between its frequency and the closest violin mode. When Dnu=0 we have the tuning condition. Here we have two resonance conditions because there are two violin frequencies very close to the drum one.

The thermal noise of the coupled system (case B, blue curve) near these frequencies is shown in the Figure 4-5 compared with the uncoupled case (red curve). The blue plot is similar to the real case measured in the input mirror of the North arm in the Virgo+ interferometer.

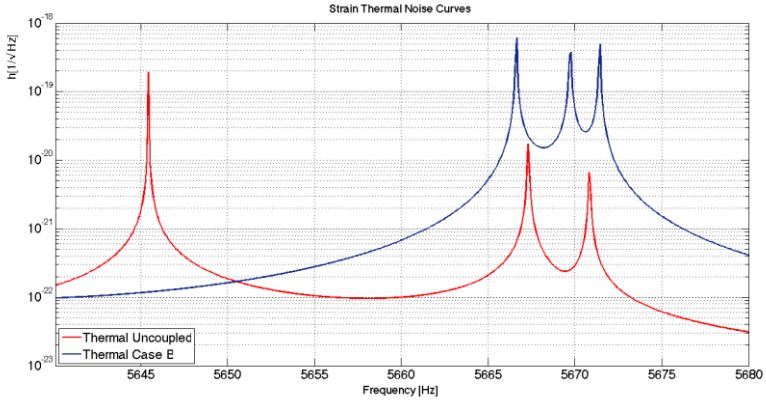

Figure 4-5: Thermal noise in the uncoupled and coupled case (B)

As shown in the Table 4-1 the quality factors of the three coupled peaks are 1.7 10^6, 1.2 10^6, 1.7 10^6 (case B, blue curve), while for the uncoupled case we have 40 10^6, 1.0 10^6, 1.0 10^6. In Figure 4-6 we shown the thermal noise curve for the two cases. The evaluation is done in the case of the coupling between the drum mode and the violin mode (case B) and compared with the predictions

using the bulk loss angle (uncoupled case) and the loss angle drawn by coupled drum mode Q. The agreement is with the thermal curve computed using the bulk loss angle.

	ν_{drum} (Hz) $Q_{drum}(10^6)$	ν_{viol1} (Hz) $Q_{viol1}(10^6)$	ν_{viol2} (Hz) $Q_{viol2}(10^6)$
Uncoupled	5645.0 40	5667.0 1.0	5671.0 1.0
A. drum coupled with viol1	5668.9 1.9	5666.1 1.9	5671.2 1.1
B. drum coupled with viol2	5670.8 1.7	5666.9 1.2	5670.3 1.7

Table 4-1

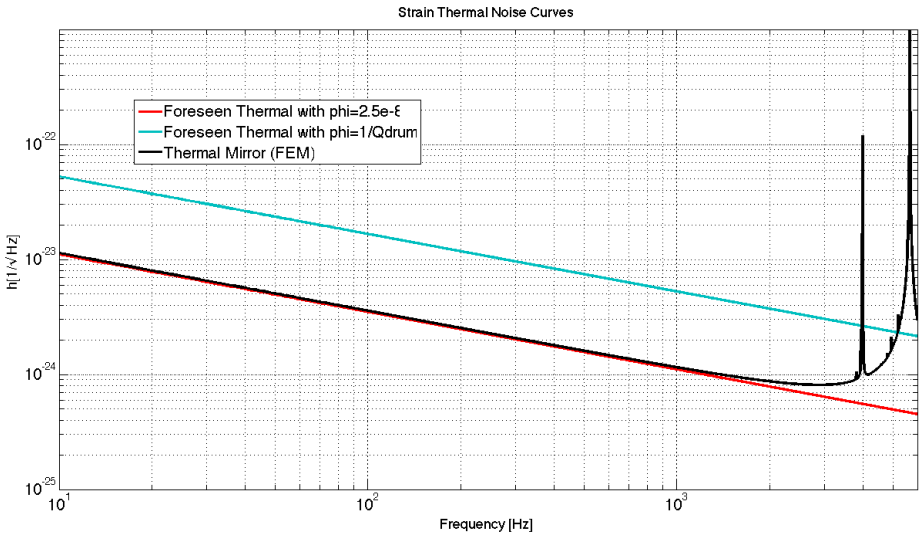

Figure 4-6: Mirror thermal noise, computed in the whole frequency range. The evaluation is done in the case of the coupling between the drum mode and the violin mode (case B) and compared with the predictions using the bulk loss angle and the loss angle drawn by coupled drum mode Q. The agreement is with the thermal curve computed using the bulk loss angle.

We can conclude that to evaluate the thermal noise of the test mass, only the intrinsic losses of the of the bulk and the coating must be used. Any energy loss coming from a resonance mechanism exchange (like for the suspension wires) will affect only the quality factors around the involved resonances but will have negligible effect elsewhere.

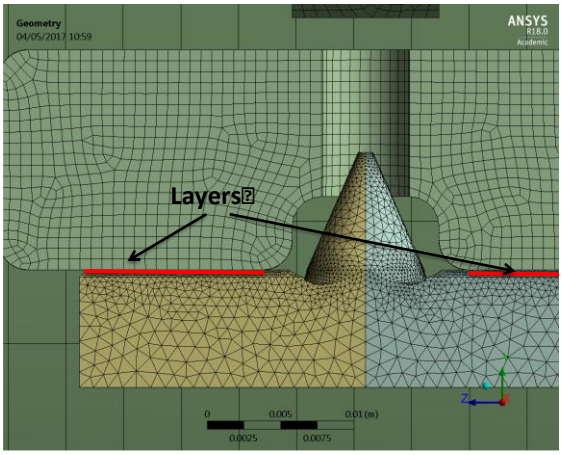

Figure 4-7: Silicate bonding layers between anchors and ears

5 Effect of the thickness of the bonding layers on thermal noise

One of the variables during the monolithic assembly procedure is the thickness of the bonding layers between the anchors and the ears. For this reason we have studied what can be the effect on the mirror and pendulum thermal noise by varying such a thickness.

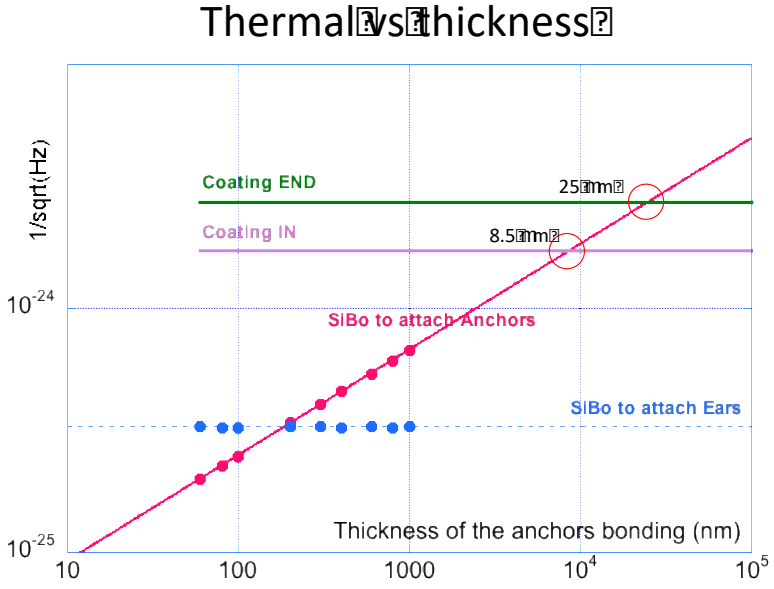

Figure 5-1: Strain thermal noise at 100 Hz of the anchors layers vs their thickness. As a comparison the ear bonding and mirror coating thermals are plotted.

In the Figure 5-1 the thermal noise at 100 Hz of the anchors layers is plotted vs their thickness. These results are compared with thermal levels of the ears silicate bondings and the coating layers on the test masses. It is shown that if the thickness is greater than 8.5 μm, the thermal of the anchors bondings starts to dominate on the overall thermal noise of the mirrors.

We have done a similar study at 10Hz, where the thermal of the anchors bonding can influence the pendulum thermal. In this case the pendulum thermal is reached at a thickness of about 4 μm.

The conclusion of this study is that, to be in a safe condition it is crucial that the anchors layers thickness does not exceed a thickness of 1 μm.

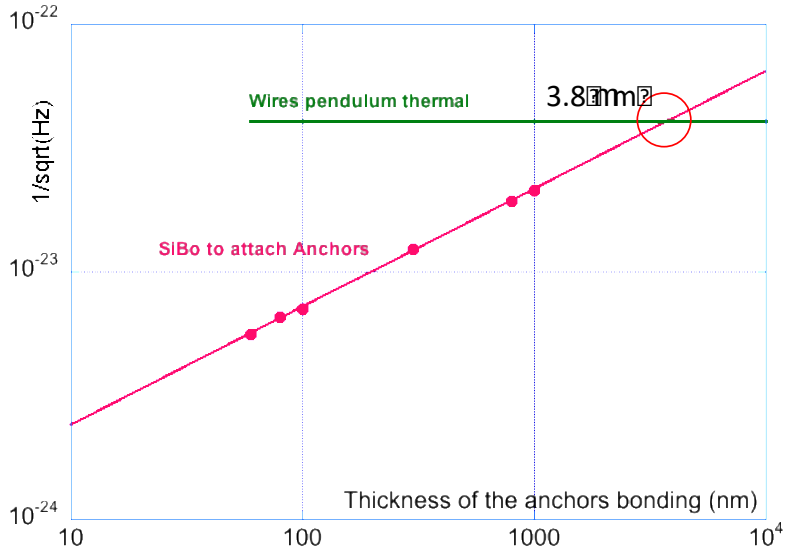

Figure 5-2: Strain thermal noise at 10 Hz of the anchors layers vs their thickness. As a comparison the pendulum thermal is plotted.

5.1 Effect of the ears damages on the contact zones of the anchors

Due to the several breaking accidents occurred on the Advanced mirrors [5][6][7], some damages are present on the mirror ears, at the level of the attaching points of the anchors. These damages are a kind of small holes on the ears having various shapes and depth. As a consequence, the polishing of some zones in the ears is compromised and it could happen that during the bonding procedure an excess of glue can fill these holes. For this reason, the thickness of the silicate bonding layers can increase in some zones. We have evaluated if the small zones of thicker deposits can be effective on the thermal noise of the test masses.

From an accurate inspection of the damaged ears we have seen that the defect holes can extend up to 10% of the overall bonded area of the anchors and can be about 100 μm deep. So, we have studied three different defects geometry as shown in the picture.

Case 1: This defect has an area of **4 mm²** which is about 0.7% of bonding area between the anchors and the ear (580 mm²)(Figure 5-3), the predicted thermal noise at 100Hz is 2.5 10^{-22} m/Hz$^{1/2}$. For several defects of this shape, covering 10%(58 mm²) of the bonding area we have:

$$\mathbf{9.7\ 10^{-22}\ m/Hz^{1/2}}$$

Case 2: This defect has an area of **19 mm²** (Figure 5-4), the predicted thermal noise at 100Hz is 5.8 10^{-22} m/Hz$^{1/2}$. For several defects of this shape, covering 10% of the bonding area we have:

10 10^{-22} m/$Hz^{1/2}$

Case 3: This defect has an area of **19 mm^2** (Figure 5-4). In this case we have considered three possible configurations:

a. all the glue filling the defect and attached to the ear

b. all the glue filling the defect but detached from the ear

c. all the glue filling the defect but attached only on the lateral surface of the cylinder.

The predicted thermal noise at 100Hz for defects covering 10% of the area we have:

a. 7.7 10^{-22} m/$Hz^{1/2}$

b. 2.3 10^{-22} m/$Hz^{1/2}$

b. 3.7 10^{-22} m/$Hz^{1/2}$

These results the following comments:

1. A recommendation is not to fill the holes with the glue;

2. Thermal noise is depending not linearly with area, as the presence of other thinner glue on the hole border is better.

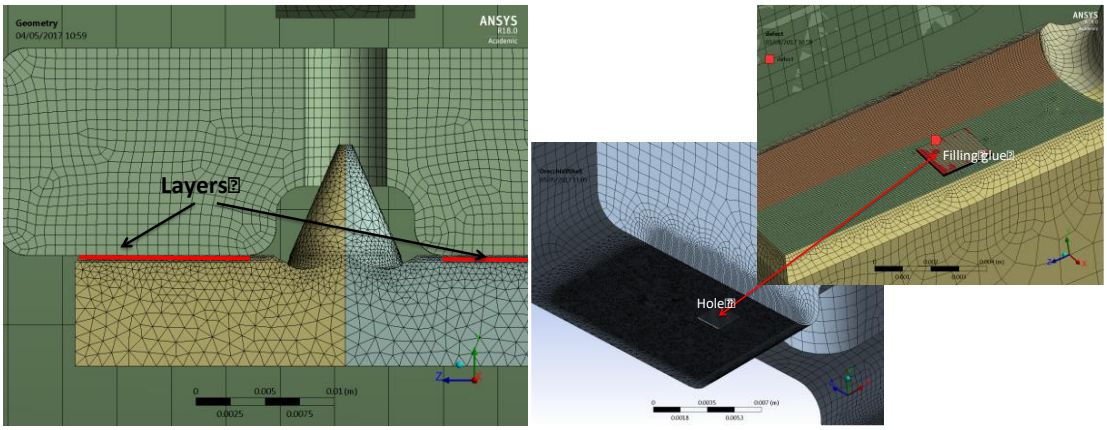

Figure 5-3. On left: anchor layers, where a defect can be present. Rigth: case 1. The defect is a hole in the ear having a squared area (4 mm^2) and 0.1 mm thick.

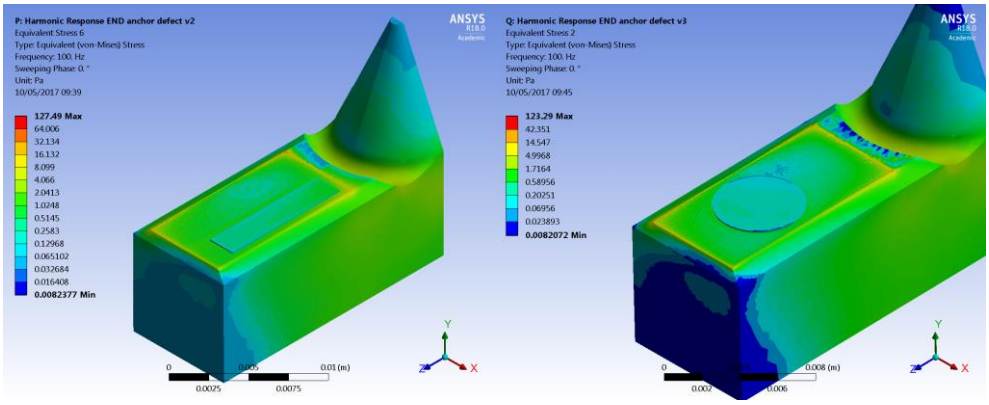

Figure 5-4. Left: case 2. The defect has a rectangular area with a dept of 0.1mm. Right : circular defect.

6 Bonding layers loss effect on the quality factors of the modes. Evaluation up to 70 kHz.

The silicate bonding losses must be included in the computation of the overall Q of the mirror because they give a non-negligible loss contribution especially at frequencies above 20kHz.

We have already shown which are the quality factors associated to the layers (see Table 3-10) and (Table 3-5)

The main contributions of such losses come from the ears bondings (see Figure 6-1, yellow dots) which play a crucial role in reducing the overall mirror Q with respect to the expected one only due to the coating (see Figure 6-1, blue and red dots).

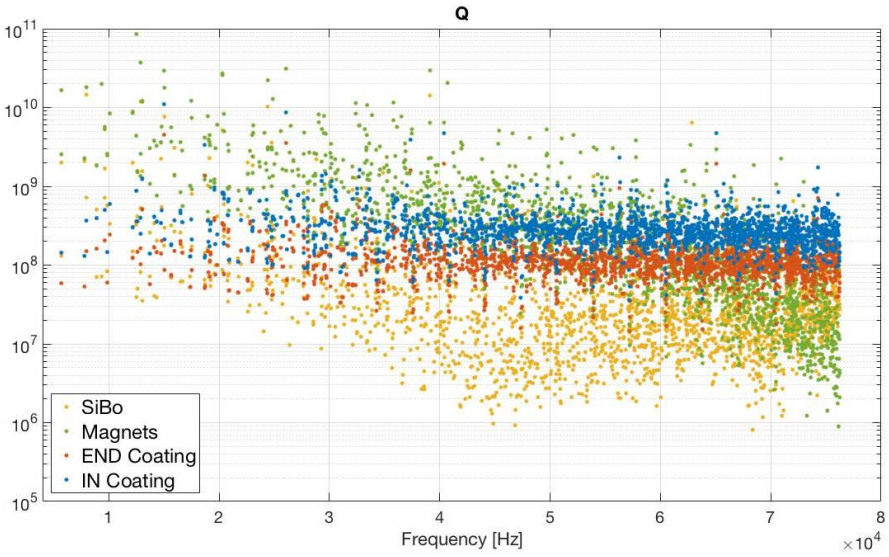

Figure 6-1: Contribution of the losses of the various silicate bonding layers.

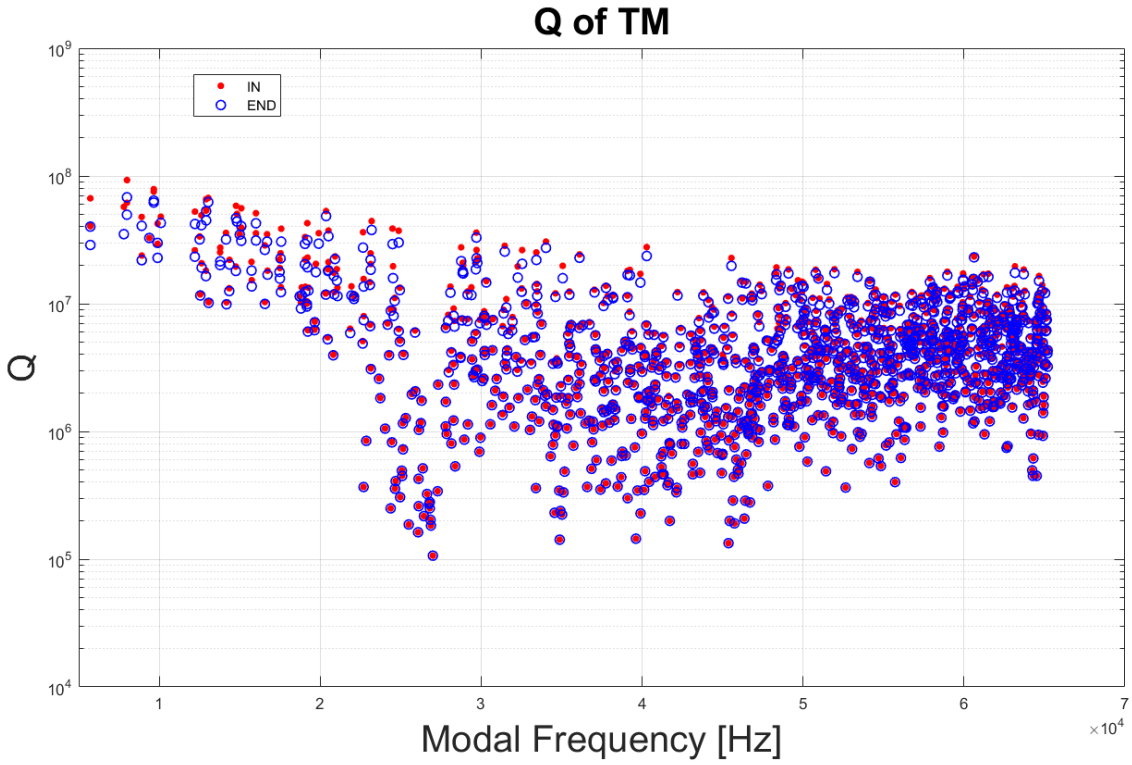

7 References

[1] M. Colombini, E. Majorana, I. Nardecchia, P. Puppo, P. Rapagnani, F. Ricci, *Virgo+ thermal noise studies*, VIR-0074B-12, 2012.

[2] A. Conte, R. De Rosa, L. di Fiore, E. Majorana, V. Mangano, L. Naticchioni, D. Pascucci, P. Puppo, P. Rapagnani, F. Ricci, 'Characterization of the mirror internal losses of the suspended test masses by means of an interferometric sensor: results on the virgo+ payloads and perspective', VIR-0475A-13.

[3] P. Rapagnani for the Pay Team, *Monolithic suspensions: outcome of the tests on the ears and proposed solutions,* VIR-0332A-14.

[4] P. Rapagnani, P. Puppo, F. Travasso, H. Vocca, E. Majorana, F. Piergiovanni, M. Montani, A. Viceré, *Lower clamps design modification for test-mass payloads*, VIR-0463A-14.

[5] VIR-0199A-17.pdf ,Monolithic Suspension Update, 21/3/2017 (pdf document)

[6] VIR-0537A-16.pptx, Monolithic issue update, 1/12/2016 (presentation)

[7] VIR-0475A-16.pptx Monolithic suspension issue 18/10/2016 (presentation)

[8] M. Punturo, *The Virgo sensitivity curve.* VIR-NOT-PER-1390-51.

[9] P. Puppo, *Virgo+MS sensitivity curve.* VIR-0639E-09.

[10] F. Piergiovanni, M. Punturo and P. Puppo, *The thermal noise of the Virgo+ and Virgo Advanced Last Stage Suspension (The PPP effect),* Virgo Note VIR-015C-09, 2009.

[11] J. E. Logan, N. A. Robertson, J. Hough, *An investigation of limitations to quality factor measurements of suspended masses due to resonances in the suspension wires*, PLA, Volume 170, Issue 5, 16 November 1992, Pages 352–358.

[12] Heptonstall A. et al, *CO_2 laser production of fused silica fibers for use in interferometric gravitational wave detector mirror suspensions*, RSI 82 011301 (2011).

[13] Y. Levin, *Phys. Rev. D*, **57**, 659-663, 1998
[14] Ansys, Inc. Corporate Homepage: www.ansys.com
[15] Cunningham L. et al. LIGO-DCC T0800163-01
[16] P. Murray, *"*Measurement of the Mechanical Loss of Test Mass Materials for Advanced Gravitational Wave Detectors*"*, Phd Thesis, (2008).
[17] R. Flaminio, D. Forest, M. Granata, B. Lagrange, C. Michel, L. Pinard, B. Sassolas, G. Cagnoli, J. Degallaix, V. Dolique, *Characterization and direct thermal noise measurement of coatings*, GWADW 2013 Elba –May 2013.
[18] I. Fiori et al, *Seismic Noise Studies with run E2 data: a first attempt to monitor daily variation*, VIR-NOT-FIR-1390-212, 2002.
[19] Virgo Collaboration*, Advanced Virgo Technical Design Report,* VIR-0128A-12 (2012).
[20] Bernardini A., Majorana E. ,Puppo P. ,Rapagnani P. , Ricci F., Testi G. *Suspension last stages for the mirrors of the Virgo interferometric gravitational wave antenna.*, Rev. Sci. Instr. 70, no. 8 (1999): 3463.
[21] G. Cagnoli and P.A. Willems, *Effects of nonlinear thermoelastic damping in highly stressed fibers*., Phys. Rev. B, 65, 174111.
[22] G. Cagnoli et al, Rev. Sci. Instr., 69, 2777-2780, 1998.
[23] S. Frasca et al, *Electromagnetic coupling dissipation between mirrors and reaction masses in Virgo,* Phys. Lett. A, 252, 11116, 1999.
[24] *http://lhocds.ligo-wa.caltech.edu:8000/advligo/GWINC*.
[25] P. Rapagnani: Il nuovo Cimento v5, n4, 1982, p385.
[26] Majorana E., Ogawa Y. «Mechanical thermal noise in coupled oscillators.» *Physics Letters A* 233 (August 1997): 162-168.
[27] A. Gillespie and Raab, Physical Review D, 52 (1995) 577.
[28] Bondu, et al. Physics Letters A 246 (1998) 227-236.
[29] Y. Levin, Phys. Rev. D, 57 (2), 659-663 (1998).
[30] *The Noise Budget of Virgo+ with Monolithic Suspensions*, VIR-0677E-09.
[31] Saulson & Gonzalez, J. Acoust. Soc. Am., 96, July 1994.
[32] K. Yamamoto, PhD Thesis, Univ. of Tokyo (2000).
[33] P. Astone, A. Colla, E. Cuoco, S. D'antonio, S. Frasca, C. Palomba, Update on NoEMi and the Lines Database (VIR-0091A-11).
[34] VIR-0622A-10, VIR-0031A-11, 'Q measurements on Monolithic Suspensions'.
[35] Andri M. Gretarsson and Gregory M. Harry et al, Dissipation of mechanical energy in fused silica fibers, RSI, 70,10,1999.
[36] Swinkels, Ruggi, Colombini, di Pace, logbook entry (28279).
[37] P. Puppo, 'A Finite Element Model of the Virgo Mirrors', VIR-NOT-ROM-1390-262.
[38] M. Punturo, 'Mechanical simulation of the Virgo+ mirrors', VIR-0556A-10.
[39] Logbook entries: 29903, 29856, 29748.
[40] F. Piergiovanni, VIR-0218A-11.
[41] Richard Day, Antonino Chiummo, VIR-0555A-11.
[42] S. Penn et al, Mechanical Loss in Tantala/Silica Dielectric Mirror Coatings, Class. Quantum Grav. 20, (2003), 2917-2928.
[43] L. Cunningham et al, PLA 374, 3993-3998, (2010).
[44] A. Dari et al, 2010 Class. Quantum Grav. 27 045010.
[45] Monolithic Suspension Change Request, (virchrq2803008).